Simulations of plasmas driven by laser wavelengths in the 1.064—10.6 μm range for their characterization as future extreme ultraviolet light sources

View Online   Export Citation   CrossMark

D. J. Hemminga,[1,2] (iD) O. O. Versolato,[1,2] (iD) and J. Sheil[1,2,a] (iD)

AFFILIATIONS

[1]Advanced Research Center for Nanolithography, Science Park 106, 1098 XG Amsterdam, The Netherlands

[2]Department of Physics and Astronomy, and LaserLaB, Vrije Universiteit Amsterdam, De Boelelaan 1081, 1081 HV Amsterdam, The Netherlands

[a]Author to whom correspondence should be addressed: j.sheil@arcnl.nl

ABSTRACT

We characterize the properties of extreme ultraviolet (EUV) light source plasmas driven by laser wavelengths in the $\lambda_{laser} = 1.064 - 10.6\,\mu m$ range and laser intensities of $I_{laser} = 0.5 - 5 \times 10^{11}$ W cm^{-2} for $\lambda_{laser} = 1.064\,\mu m$. Detailed numerical simulations of laser-irradiated spherical tin microdroplet targets reveal a strong laser-wavelength dependence on laser absorptivity and the conversion efficiency of generating in-band EUV radiation. For $\lambda_{laser} = 1.064\,\mu m$ irradiation, the increase in in-band radiation with increasing laser intensity is offset by only a minor reduction in conversion efficiency. Radiative losses are found to dominate the power balance for all laser wavelengths and intensities, and a clear shift from kinetic to in-band radiative losses with increasing laser wavelength is identified. Yet, with increasing laser intensity, such a shift is absent. We find that the existence of a maximum conversion efficiency, near $\lambda_{laser} = 4\,\mu m$, originates from the interplay between the optical depths of the laser light and the in-band EUV photons for this specific droplet-target geometry.

I. INTRODUCTION

Extreme ultraviolet lithography (EUVL) is driving mass production of today's most advanced integrated circuits (ICs).[1,2] Crucial to the success of this technology has been the development of a sufficiently powerful, stable, and "clean" source of EUV radiation[3] concentrated in a narrow 13.5 nm $\pm$ 1% region where molybdenum/silicon multilayer mirrors exhibit high reflectance (the so-called "in-band" region).[4,5] This radiation is most efficiently generated in a laser-produced plasma (LPP) formed when high-intensity CO_2 laser light (laser wavelength $\lambda_{laser} = 10.6\,\mu m$) is focused onto pre-shaped tin microdroplet targets.[6–12] This plasma contains large populations of Sn^{11+} $-$ Sn^{15+} ions, which generate intense, narrowband EUV radiation through bound–bound atomic transitions.[13–19]

Nowadays, industrial EUV sources generate a remarkable 250 W of in-band EUV power.[20] Efforts to increase source powers beyond 600 W are now under way to facilitate increased wafer throughput.[21] While CO_2 laser-driven plasmas are the backbone of current EUV sources for high-volume manufacturing,[3,22] rapid developments[23] in solid-state lasers (which typically operate in the near- to mid-infrared wavelength range) make them a viable alternative[24–26] in the future due to their high efficiencies in converting electrical power to laser light and their potential for scaling to high average powers.[23,27] These developments have sparked significant interest in the study of short-wavelength laser-driven plasmas for nanolithography.[24–26]

Two crucial topics to be addressed in such studies are the impact of (i) laser wavelength λ_{laser} and (ii) laser intensity I_{laser} on the radiative and kinetic properties of the plasma. The kinetic properties are especially important in the context of debris generation,[28,29] which may limit the lifetime of optical components. The laser wavelength sets the critical electron density (the density at which the plasma becomes opaque to incident laser radiation) according to $n_{e,cr} \propto \lambda_{laser}^{-2}$. This determines the densities for which EUV radiation is generated and must propagate through. High plasma densities or long path lengths generate large optical depths, which redistribute in-band energy into other

channels, e.g., via spectral broadening.[30] While this effect can be negated by moving to long laser wavelengths,[31] the presence of steep electron density gradients in the plasma can lead to significant laser reflection from the critical surface and a loss of input laser energy.[32,33] Efficiency at different laser wavelengths is, therefore, determined by a trade-off in numerous underlying physical processes. The goal of the present work is to quantify this trade-off for laser wavelengths lying in the largely unexplored region between $\lambda_{laser} = 1.064 \, \mu m$ (Nd:YAG laser) and $10.6 \, \mu m$, although the existence of an optimum laser wavelength has been suggested previously in the EUV source community.[34,35] Furthermore, we aim to quantify the effect of a second trade-off between absolute power output and the efficiency of generating in-band radiation during illumination by a range of laser intensities.

In this article, we present a comprehensive characterization of the properties of laser-produced EUV source plasmas. The parameter space encompasses (i) laser wavelengths in the $1.064 \leq \lambda_{laser} \leq 10.6 \, \mu m$ range coupled with an optimum intensity scaling $I_{laser} \propto \lambda_{laser}^{-1}$ and (ii) laser intensities in the $0.5 \times 10^{11} \leq I_{laser} \leq 5 \times 10^{11}$ W cm^{-2} range for $\lambda_{laser} = 1.064 \, \mu m$. We identify a strong laser-wavelength dependence on laser absorptivity and EUV generation efficiency, and, moreover, report on the early time establishment of steady-state plasma flows. The partitioning of laser power into plasma components (kinetic, internal, and radiated power) is quantified. In our case study, we delve into the factors underlying a maximum in the conversion efficiency (ratio of in-band power radiated into the laser-illuminated half-sphere to laser power) for $\lambda_{laser} \approx 4 \, \mu m$ laser irradiation, a promising wavelength region indicated previously.[34] It should be emphasized that this is *not* a global optimum; higher conversion efficiencies may be achieved at longer wavelengths by optimizing laser absorption by intricate target preparation,[20] which is not discussed in the presented case study. The partitioning of laser power into the plasma components is also quantified as a function of the laser intensity, where only weak dependencies are found for the kinetic and radiated power. Moreover, we report on the spatial profiles of various plasma parameters (temperature, electron density etc.) while the plasma exhibits steady-state flow. Finally, we observe an increase in in-band radiative power with increasing laser intensity at only a small cost to the overall efficiency.

II. NUMERICAL SIMULATIONS

We have performed numerical simulations of laser-produced tin plasmas using the two-dimensional radiation-hydrodynamics code RALEF-2D.[36–38] It has proven to be a powerful modeling capability for EUV source plasmas, providing useful insights on various topics such as tin droplet fragmentation,[39] droplet propulsion and deformation,[11,40] plasma properties,[19,33] and late-time plasma expansion.[29] In the following, we provide details of the code and the simulation parameters used in this study.

A. Code description

RALEF-2D solves the equations of single-fluid, single-temperature hydrodynamics including the processes of radiation transfer and thermal conduction. The hydrodynamic component of RALEF-2D is based on an upgraded version of the 2D CAVEAT code,[41] where the hydrodynamic equations are solved on a structured quadrilateral mesh using a second-order Godunov-type scheme. Radiation transfer, which is implemented using a symmetric semi-implicit method with respect to time discretization,[42,43] is modeled using the quasistatic, local thermodynamic

equilibrium (LTE) radiation transport equation.[33] As in our previous works,[11,29] the angular dependence of the radiation intensity is modeled using the S_n quadrature method with $n = 6$. The spectral absorption coefficients required to solve this equation are derived from steady-state collisional-radiative modeling using the THERMOS code.[44,45]

The equation-of-state of tin was constructed using the Frankfurt equation-of-state (FEOS) model,[46–48] which can model both low-temperature liquid–gas phase coexistence regions and high-temperature plasma states.[33] Laser light absorption and reflection are treated using a hybrid model combining a geometrical-optics ray-tracing approach in low-density plasma regions and a wave-optics approach in regions near and beyond the critical electron density.[49] Laser absorption coefficients are derived from the complex dielectric permittivity of the plasma as per the Drude model.[50]

B. Simulation parameters

The simulated cases consider laser irradiation of 30-μm-diameter liquid tin droplets, close to the industry standard, with spatially constant laser fluences of 60 μm in width. The laser pulses are temporally trapezoidal shaped with pulse lengths of 20 ns (rise and fall times of 0.2 ns). These experimental parameters are prototypical for recent simulation and experimental works alike (see, e.g., Refs. 9, 25, 30, 32, 33, and 51–57). The laser wavelengths considered in the first part of this work are $\lambda_{laser} = 1.064, 2, 3, 4, 5, 7$, and $10.6 \, \mu m$. This encompasses two distinct regimes of laser absorption, where absorption occurs primarily in the (i) underdense corona (for small λ_{laser}) or (ii) a narrow region near the critical surface (for long λ_{laser}).[32] The laser intensity is scaled according to $I_{laser} = (1.4 \times 10^{11})/\lambda_{laser}$ W cm^{-2}, an experimentally motivated scaling, which yields high conversion efficiencies for the laser wavelengths considered in this study.[25,51,58] We note the close similarity between this scaling and the optimum laser intensity $I_{laser} \propto \lambda_{laser}^{-1.2}$ proposed by Nishihara *et al.*[59] In the second part of this study, we keep the laser wavelength fixed at $\lambda_{laser} = 1.064 \, \mu m$ and vary the laser intensity in the range $I_{laser} = 0.5 - 5 \times 10^{11}$ W cm^{-2} to probe its effect on the radiative and kinetic properties of the plasmas.

III. WAVELENGTH-DEPENDENT PLASMA DYNAMICS

In Fig. 1, we provide a still of the plasma formation induced by the four laser wavelengths $\lambda_{laser} = 1.064, 2, 4, 10.6 \, \mu m$ at the time $t = 18$ ns after the laser pulse is switched on. The absorbed laser power per unit volume normalized by the input laser power, denoted as ζ_{abs}, is shown in the upper halves of the panels. We find that with increasing λ_{laser}, the laser absorption zone moves further away from the droplet (dark blue region) due to the inverse square dependence of $n_{e,cr}$ (black contours) on λ_{laser}, and that the electron density closely follows the profile $n_e \propto d^{-2}$ (where $d = \sqrt{r^2 + z^2}$) associated with a steady spherical flow.[33] Moreover, the spatial extent over which the laser light is absorbed reduces with increasing λ_{laser}, a direct result of the aforementioned transitioning between the two distinct regimes of laser absorption. The steep electron density gradient precludes efficient absorption of long-wavelength laser light. In panel (d), we see that CO_2 laser absorption is restricted to a narrow region in front of the critical surface. Adopting the Kramers's cross section for inverse bremsstrahlung and assuming a (i) constant-temperature laser absorption zone and a (ii) $n_e \propto d^{-2}$ profile, the optical depth of laser light τ_{laser} can be written as[33]
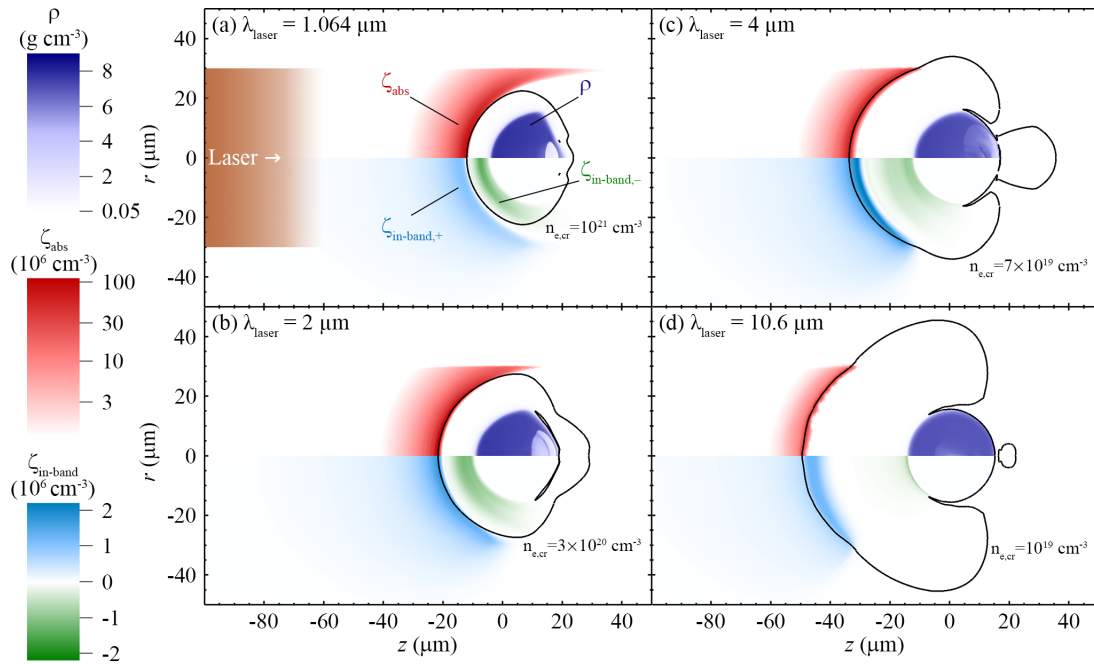
FIG. 1. Instantaneous (at $t = 18$ ns) volume-specific laser deposition rate[49] normalized by the input laser power ζ_{abs} (red) and in-band radiative power normalized by the input laser power $\zeta_{in-band}$ (light blue–green) normalized by the input laser power for $\lambda_{laser} =$ (a) 1.064, (b) 2, (c) 4, and (d) 10.6 μm. The critical electron density (black contour) and fluid density ρ (dark blue) are indicated.

$$\tau_{laser} \approx 4 \times 10^{-3} \frac{Z \ln(\Lambda)}{T^{3/2} \lambda_{laser}^2} \frac{R_{mc}}{a_{uv}^3}, \tag{1}$$

where Z, $\ln(\Lambda)$, T, R_{mc}, and a_{uv} are the charge state, Coulomb logarithm, temperature (in hundreds of eV), radius of the critical surface, and a dimensionless parameter determining the position of laser absorption. Inferring appropriate values from our simulations, we estimate $\tau_{1.064\mu m} \sim 10$ and $\tau_{10.6\mu m} \sim 1$ for the present illumination geometry.

In the bottom halves of Fig. 1, we show the net in-band radiated power per unit volume normalized by the input laser power, denoted as $\zeta_{in-band}$ and labeled "+" for net emission and "−" for net absorption. This provides a local measure of the efficiency of converting laser light to in-band radiation. Of the four cases shown, the 4 μm-driven plasma exhibits the highest $\zeta_{in-band,+}$. We see that with increasing λ_{laser}, the region of net in-band emission $\zeta_{in-band,+}$ (light blue regions) moves from regions with $n_e < n_{e,cr}$ to regions with $n_e > n_{e,cr}$. Furthermore, the regions of net absorption of in-band radiation (dark green regions) are located close to the droplet (a region with high density and low temperature). As discussed by Sunahara et al.,[60] the long mean free paths associated with such radiation can heat the high-density region and enhance the mass ablation rate.[61,62]

A. Establishment of steady-state plasma flow

The instantaneous partitioning of laser power during $\lambda_{laser} = 4$ μm illumination is shown in Fig. 2. In Fig. 2(a), we show the input P_{las} (black), absorbed P_{abs} (blue), reflected P_{ref} (orange), and "escaped" P_{esc} (brown) laser power components. The escaped
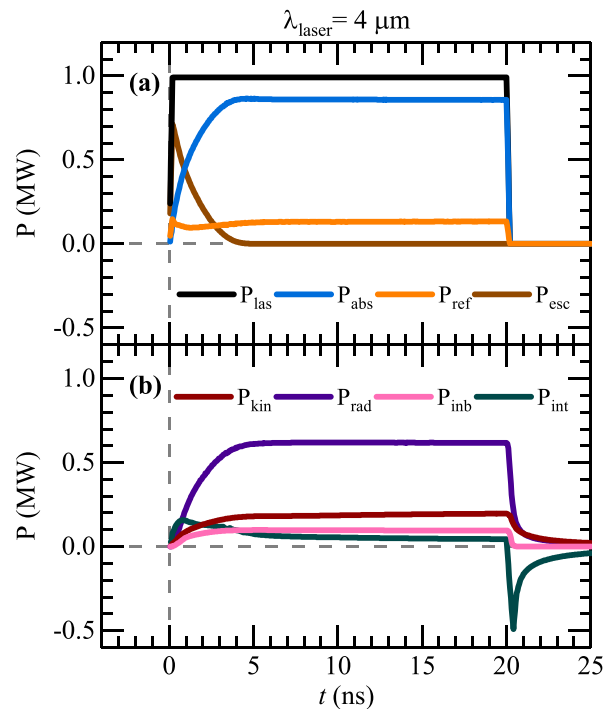
FIG. 2. Time-dependent partitioning of laser power into (a) laser- and (b) plasma-based components for $\lambda_{laser} = 4$ μm irradiation of a 30-μm-diameter tin droplet.

component represents laser radiation that initially misses the target, a quantity which decreases rapidly as the plasma expands and starts absorbing incident laser radiation. After 5 ns, a "steady-state" plasma flow regime is established whereafter P_{abs} and P_{ref} attain near-constant values. This behavior is evident in the plasma-based components P_{kin} (kinetic power, red), P_{rad} (total radiated power, purple), P_{inb} (in-band power, pink), and P_{int} (internal power—derived from the specific Helmholtz free energy,[46] green) shown in Fig. 2(b). It is well-known that plasmas containing high-Z ions exhibit large radiative losses,[63] and our simulations indicate that approximately 70% of the absorbed laser power is channeled into radiation. Moreover, we find that nearly 16% of this radiation is concentrated in the in-band region, a surprisingly large fraction given the narrowness (0.27 nm) of this wavelength region.

B. Wavelength-dependent power partitioning

Next, we quantify power partitioning as a function of laser wavelength. This enables a comprehensive characterization of the EUV plasma source conditions, where high laser absorptivities coupled with large in-band radiative losses and minimal kinetic losses are most desired. In Fig. 3(a), we present the ratios P_{abs}/P_{las} (blue) and P_{ref}/P_{las} (orange) as a function of laser wavelength at steady-state conditions. We note the significant increase in laser reflectivity comparing $\lambda_{laser} = 1.064$ and $10.6\,\mu m$ cases, which is due to the significant reduction of τ_{laser} with increasing λ_{laser} specific to the current target geometry.

The internal, radiated, and kinetic components exhibit their own unique dependencies on laser wavelength. In Fig. 3(b), we show the ratios P_{rad}/P_{abs} (purple squares), P_{kin}/P_{abs} (red circles), P_{inb}/P_{abs} (pink triangles), and P_{int}/P_{abs} (green inverted triangles). The dashed curves represent power-law fits to the data. The origin of these power laws is not exactly known, and they most likely originate from a complex interplay of radiation transport, laser absorption, and plasma expansion effects. With increasing λ_{laser} (and therefore decreasing plasma density), the optical depth of EUV photons reduces from $\tau_{EUV} \approx 6$ (Nd:YAG-driven plasma) through $\tau_{EUV} \approx 2$ (4-μm-driven plasma) to $\tau_{EUV} \approx 0.5$ (CO$_2$-driven plasma).[30,33] This limits the degree of spectral broadening and redistribution of in-band energy into other channels, which explains the observed increase in P_{inb}/P_{abs} with increasing λ_{laser} and the behavior of the spectral purity SP$_P$ = P_{inb}/P_{rad} (defined in the full 4π) presented in Fig. 3(c). The influence of optical depth on spectral purity and conversion efficiency is further discussed in the work of Schupp et al.[25,30] As the relative fraction of radiative losses increases with increasing λ_{laser}, the balance dictates a corresponding decrease in kinetic losses.

The efficiency of producing in-band EUV radiation as a function of laser wavelength is shown in Fig. 3(c). The conversion efficiency CE$_P$ (black squares) exhibits a concave dependence on λ_{laser} with a maximum at $\lambda_{laser} = 4\,\mu m$. This maximum arises from the rather unique combination of the values of laser optical depth and optical depth of EUV photons. In essence, the plasma conditions are in a "sweet spot" intermediate to the extreme cases of high laser absorptivity/low spectral efficiency ($\lambda_{laser} = 1.064\,\mu m$) and low absorptivity/high spectral efficiency ($\lambda_{laser} = 10.6\,\mu m$). This explains the simulation results of Langer et al., who identified an optimum for $\lambda_{laser} = 4.5\,\mu m$ irradiation of a one-dimensional tin vapor target,[34]
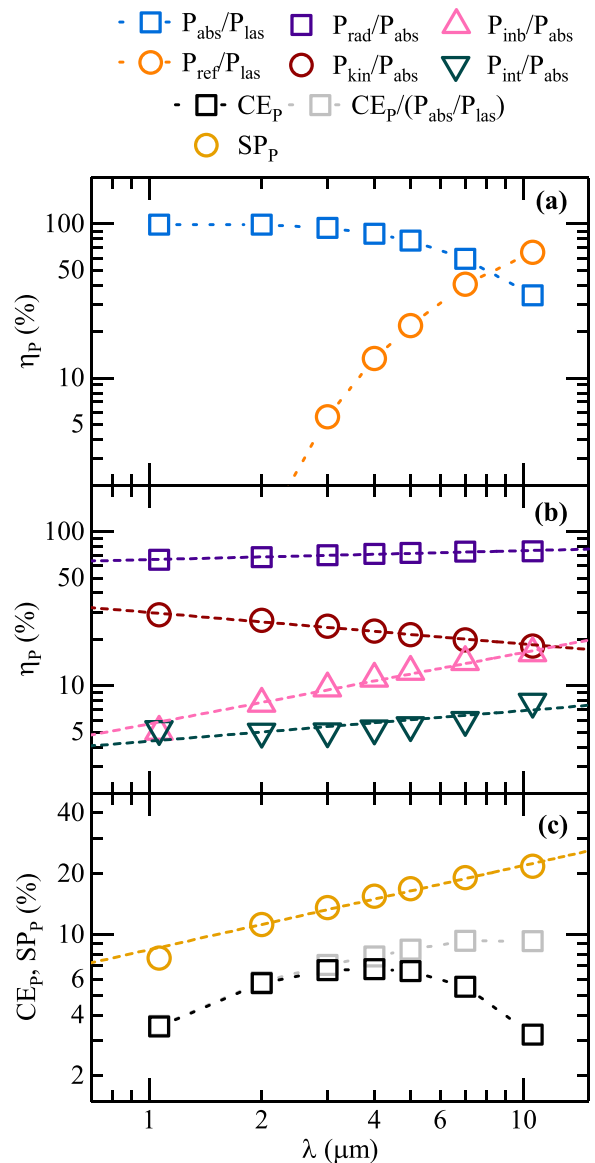
FIG. 3. Instantaneous (at $t = 18$ ns) partitioning of (a) laser-based components (normalized by P_{las}) and (b) plasma-based components (normalized by P_{abs}), and (c) spectral purity SP$_P$ (yellow circles), conversion efficiency CE$_P$ (black squares), and CE$_P/(P_{abs}/P_{las})$ (gray squares) as a function of laser wavelength. The dashed curves represent power-law fits to the data.

with which our result is in agreement. It is worthwhile noting that the maximum is located on a rather flat part of the curve between 3 and 5 μm, and that the CE$_P$ increase from 1.064 to 2 μm is rather substantial, in line with experimental observations.[58]

The strong dependence of conversion efficiency on laser absorptivity for $\lambda_{laser} > 4\,\mu m$ substantiates the opportunity to improve CE$_P$ for long laser wavelengths. In Fig. 3(c), we plot the quantity CE$_P/(P_{abs}/P_{las})$ (grey squares), which represents the conversion efficiency if the absorption fraction would be unity for all laser

wavelengths. This quantity increases monotonically with increasing λ_{laser}, while reaching a plateau between $\lambda_{laser} = 7$ and $10.6\,\mu m$.

In order to increase laser absorptivity for long λ_{laser}, one could pre-irradiate the target to convert it into a rarefied, spatially extended medium. This would decrease the plasma density gradient and subsequently increase the laser optical depth and, thus, its absorption in the plasma. Such target pre-shaping has been successfully applied in industrial applications, enabling high conversion efficiencies from CO_2 laser-irradiated tin targets.[3] That said, target shaping remains unexplored in the intermediate wavelength region considered in this work, and this may lead to substantial increases in CE_P.

IV. INTENSITY-DEPENDENT PLASMA DYNAMICS

As an extension to the characterization described above, we investigate the effects of laser intensity I_{laser} on the radiative and kinetic properties of a plasma driven by $\lambda_{laser} = 1.064\,\mu m$. In a similar vein to Fig. 1, we show in Fig. 4 the tin mass density ρ, critical electron density contour $n_{e,cr}$, ζ_{abs} (absorbed laser power per unit volume normalized by input laser power), and $\zeta_{in-band}$ (in-band radiated power per unit volume normalized by input laser power) for four laser intensities $I_{laser} = \{0.5, 1.4, 2, 5\} \times 10^{11}\,W\,cm^{-2}$ at $t = 18\,ns$. With increasing laser intensity, the critical electron density contour tends toward a more spherical shape, and its radius (as measured from the center of mass of the droplet, for instance) extends to larger distances. This leads to a reduction in the amount of laser radiation that "escapes" from the system, as is visible from the upper halves of the panels in Fig. 4. In the following, we discuss and compare the properties of these plasmas in greater detail.

A. Dependence of spatial plasma features on laser intensity

As steady-state plasma flows have been attained at $t = 18\,ns$, we can compare the spatial profiles of various plasma quantities for different laser intensities. Spatial profiles, taken along the z-axis, of all relevant variables are shown in Fig. 5 for $I_{laser} = \{0.5, 2, 5\} \times 10^{11}\,W\,cm^{-2}$. The profiles generated by different laser intensities are shifted by the position of the droplet surface $z_{droplet}$, which depends on laser intensity as seen in Fig. 4. Specifically, $z_{droplet}$ is defined as the point along the z-axis where $\rho = 1\,g\,cm^{-3}$.

Examining Fig. 5(a), we see that the fluid density ρ looks similar for all laser intensities except in the region $0 < z - z_{droplet} < 10\,\mu m$, where higher laser intensities yield higher fluid densities. In tandem, the fluid speed $|\mathbf{v}|$ shows the opposite behavior in this region, where higher intensities lead to lower speeds. However, for $z - z_{droplet} > 10\,\mu m$, the expected positive correlation between flow speed and intensity is established, and fluid density profiles overlap. In Fig. 5(a), we also plot the sound speed $c_s = \sqrt{\gamma Z_{ion} k_B T / m_{ion}}$, where γ is the adiabatic index (taken to be $\gamma = 1.167$, following Ref. 32) and $m_{ion} = 118.71\,amu$ is the isotope-averaged ion mass. The position of the sonic point (where $|\mathbf{v}| = c_s$) also moves to larger distance with increasing laser intensity. Shown in Fig. 5(b) are profiles of the electron density n_e and the volume-specific laser deposition rate normalized by the input laser power ζ_{abs}, where the aforementioned shift of the

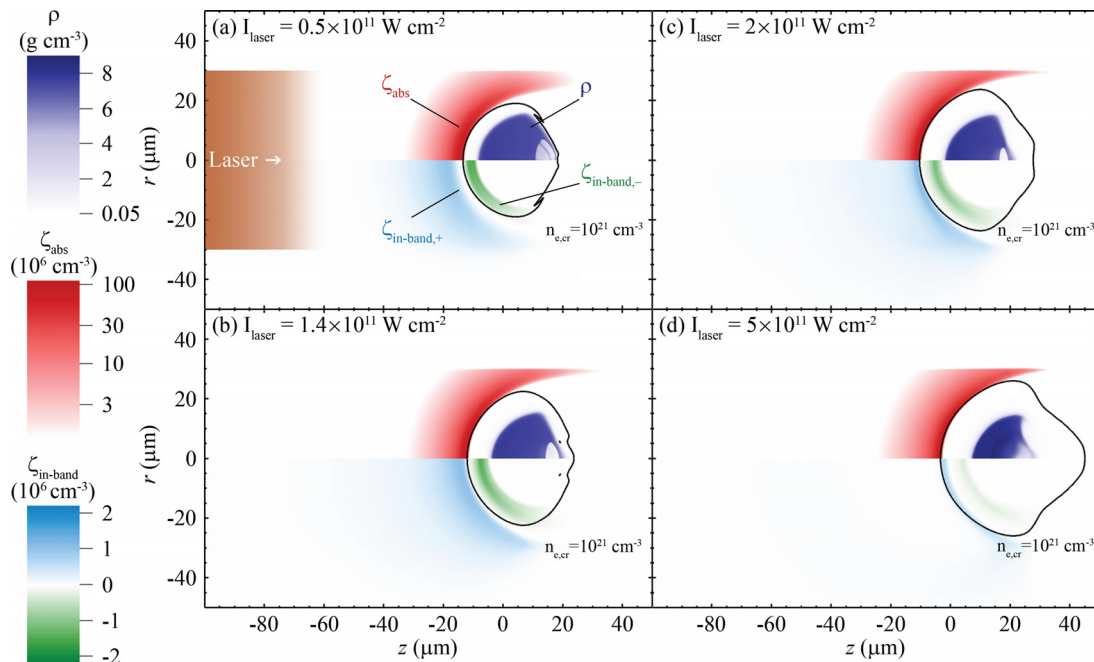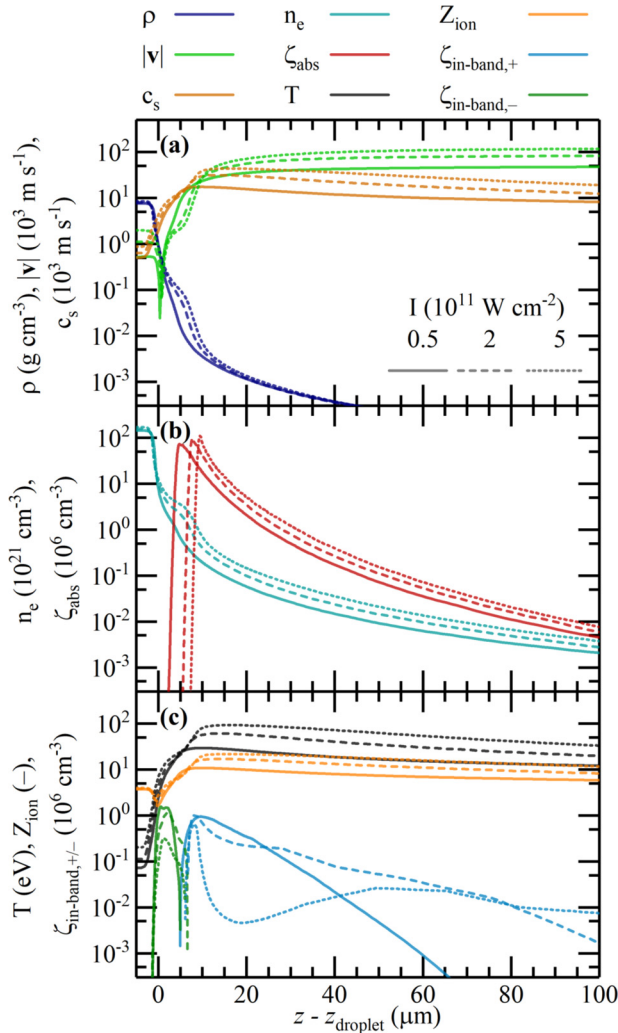**FIG. 4.** Instantaneous (at $t = 18\,ns$) volume-specific laser deposition rate[49] normalized by the input laser power ζ_{abs} (red) and in-band radiative power normalized by the input laser power $\zeta_{in-band}$ (light blue–green) normalized by the input laser power for $I_{laser} =$ (a) 0.5, (b) 1.4, (c) 2, and (d) 5 $\times 10^{11}\,W\,cm^{-2}$. The critical electron density (black contour) and fluid density ρ (dark blue) are indicated.

FIG. 5. Spatial profiles along the laser axis (at $t = 18$ ns) for three laser intensities $I_{laser} = \{0.5, 2, 5\} \times 10^{11}$ W cm^{-2} and fixed laser wavelength $\lambda_{laser} = 1.064\,\mu$m, shown as solid, dashed, and dotted lines, respectively. The profiles are shifted in space by the position of the droplet surface, $z_{droplet}$. Shown are (a) fluid density ρ (dark blue), fluid speed $|\mathbf{v}|$ (light green), and sound speed c_s (brown); (b) electron density n_e (cyan) and volume-specific laser deposition rate normalized by the input laser power ζ_{abs} (red); and (c) temperature T (black), average charge state Z_{ion} (orange), net in-band radiative emission power normalized by the input laser power $\zeta_{in-band,+}$ (light blue), and net in-band radiative absorption power normalized by the input laser power $\zeta_{in-band,-}$ (dark green).

position of the critical electron density $n_{e,cr} \approx 10^{21}$ cm^{-3} to larger distances with increasing I_{laser} is clearly observed.

The fluid temperature profiles, shown in Fig. 5(c), peak close to the positions of maximum laser absorption and are found to increase with increasing laser intensity (also see discussion in Sec. IV B). The spatial profile of the average charge state Z_{ion} shown in Fig. 5(c) follows that of the temperature, given the power law scaling $Z_{ion} \propto T^{0.6}$, see also Ref. 32. Also presented in Fig. 5(c) is the volume-specific in-band radiative power normalized by the input laser power $\zeta_{in-band}$, split into its positive (net emission) and negative (net absorption) branches. As

before, the position of net absorption $\zeta_{in-band,-}$ is located beside the droplet surface. The profile of the net emission of in-band radiation, $\zeta_{in-band,+}$, exhibits a non-trivial dependence on laser intensity: with increasing I_{laser}, the spatial profile first broadens and then, for $I_{laser} = 5 \times 10^{11}$ W cm^{-2}, exhibits a local minimum near $z - z_{droplet} = 20\,\mu$m. This behavior can be understood from the spatial profiles of the average charge state Z_{ion} and the fluid density ρ, respectively, the location and abundance of ion charge states responsible for in-band EUV emission ($11 < Z_{ion} < 14$).[19] Comparing the region $10 < z - z_{droplet} < 40\,\mu$m for the three laser intensities, the case $I_{laser} = 0.5 \times 10^{11}$ W cm^{-2} is characterized by so-called "underheating" ($Z_{ion} < 11$) toward longer distances, while $I_{laser} = 5 \times 10^{11}$ W cm^{-2} is characterized by "overheating" ($Z_{ion} > 14$) toward shorter distances.

B. Intensity-dependent power partitioning

We now quantify the power partitioning as a function of laser intensity, the results of which are shown in Fig. 6. From panel (a), we see that the absorbed power fraction remains near unity for the described intensity range. Moreover, the growth of the critical surface radius with increasing laser intensity leads to a reduction in the escaped component, while at the same time, we see an increase in the reflected component.

Rather surprisingly, the ratios of the radiated and kinetic components, shown in Fig. 6(b) as P_{rad}/P_{abs} and P_{kin}/P_{abs}, are approximately constant over the order-of-magnitude I_{laser} range considered here. Trivially, I_{laser} is proportional to the total laser power P_{las}, and from Fig. 6(a), we can deduce that P_{abs} and P_{las} are equivalent for our purpose here. As such, we will only consider the intensity scaling of P_{kin} and P_{rad} in the following, having established a simple connection to the quantities shown in Fig. 6(b), given by

$$P_{kin}/P_{abs} \propto P_{kin}I_{laser}^{-1}, \tag{2}$$

$$P_{rad}/P_{abs} \propto P_{rad}I_{laser}^{-1}. \tag{3}$$

As steady-state flow is observed, the mass flux is conserved,[33] and we can describe the system by the kinetic energy flux at any point along a flow line. We consider the scaling of kinetic energy flux with laser intensity at the sonic point. Analogous to the total laser input power argument, we consider the specific kinetic energy transfer rate I_{kin} (sometimes referred to as the kinetic energy flux density), which is proportional to the total kinetic energy transfer rate P_{kin}. The kinetic energy flux density is defined as the product of the ion number flux and the ion kinetic energy via

$$I_{kin} = \rho|\mathbf{v}| \cdot \frac{1}{2}m_{ion}|\mathbf{v}|^2 \propto \rho|\mathbf{v}|^3, \tag{4}$$

which becomes $I_{kin} \propto \rho_s c_s^3$ at the sonic point. The sonic speed $c_s \propto \sqrt{Z_{ion}T}$ can be written as a sole function of temperature T through the scaling $Z_{ion} \propto T^{0.6}$. The scaling of the temperature at the sonic point T_s with laser intensity is derived from the simulation data and is given by $T_s \propto I_{laser}^{0.49}$, in close agreement with the findings in Refs. 32 and 59. We obtain the following scaling for the kinetic energy flux density:

$$I_{kin} \propto \rho_s c_s^3 \propto \rho_s I_{laser}^{1.17}, \tag{5}$$

which is very close to a linear scaling with laser intensity. Furthermore, combining the scaling of the speed with the scaling of the density
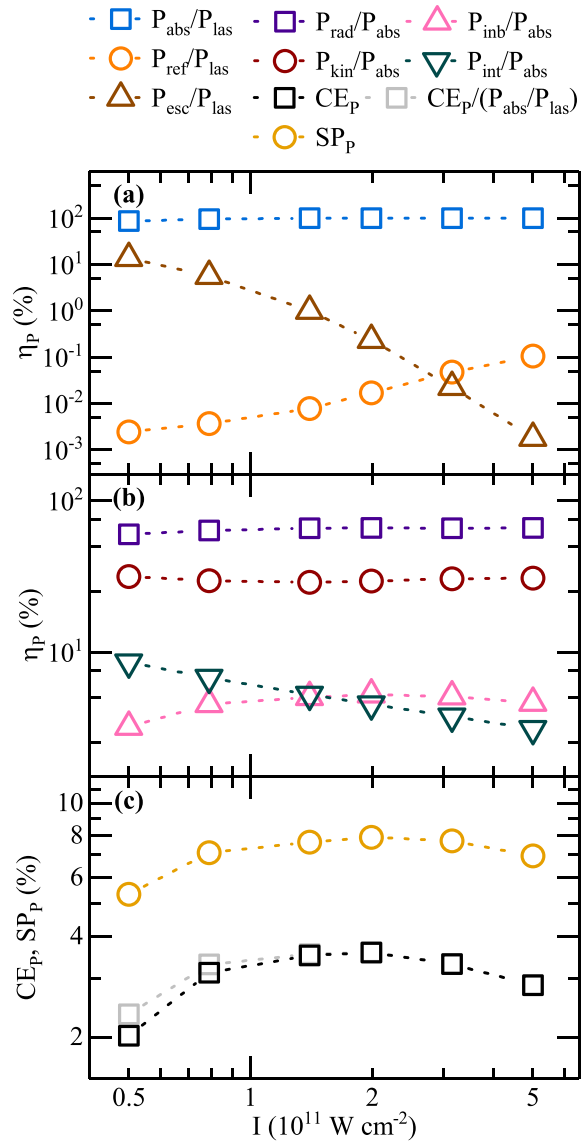
FIG. 6. Instantaneous (at $t = 18$ ns) partitioning of (a) laser-based components (normalized by P_{las}) and (b) plasma-based components (normalized by P_{abs}), and (c) spectral purity SP_P (yellow circles), conversion efficiency CE_P (black squares), and $CE_P/(P_{abs}/P_{las})$ (gray squares) as a function of laser intensity.

$\rho_s \propto I_{laser}^{-0.22}$ at the sonic point, as obtained from the simulations, we obtain $I_{kin} \propto I_{laser}^{0.95}$ to even more accurately reproduce the linear scaling with laser intensity.

By virtue of Eq. (2), we can now write

$$P_{kin}/P_{abs} \propto I_{kin} I_{laser}^{-1} \propto I_{laser}^{-0.05}, \qquad (6)$$

which underpins the observed very weak dependence of P_{kin}/P_{abs} on I_{laser} as is evident from Fig. 6(b).

Next, we consider the scaling of the radiative energy flux density, I_{rad}, which is proportional to P_{rad}. The energy density of a non-equilibrium local radiation field (as is the case in EUV

source plasmas) is often characterized by the radiation temperature $T_r = (U_r/4\sigma_{SB})^{1/4}$, where σ_{SB} is the Stefan–Boltzmann constant and

$$U_r = \int_{4\pi} \int_0^\infty I_\nu \, d\nu \, d\vec{\Omega} \qquad (7)$$

is the 4π- and frequency-integrated specific intensity of the radiation field I_ν. Clearly, one can write

$$I_{rad} \propto U_r \propto T_r^4. \qquad (8)$$

From the RALEF-2D simulations, we find the scaling $T_{r,max} \propto I_{laser}^{0.24}$ and, therefore, the following relationship holds *locally*:

$$I_{rad} \propto I_{laser}^{0.96}. \qquad (9)$$

Based on Eq. (3), we conclude that there is a near-independence of the radiation component on the laser intensity as

$$P_{rad}/P_{abs} \propto I_{laser}^{0.96} I_{laser}^{-1} \propto I_{laser}^{-0.04}. \qquad (10)$$

The dependence of conversion efficiency CE_P on laser intensity, shown in Fig. 6(c), follows the same trend as the spectral purity (SP_P) with a maximum at $I_{laser} = 2 \times 10^{11}$ W cm^{-2}. This is due to the near-independence of P_{rad}/P_{abs} and P_{abs}/P_{las} on laser intensity, the exact opposite of what was found in Sec. III B. As such, the effect of optimizing the absorption ratio by reducing the escaped laser component does not shift the found maximum as is clear from $[CE_P/(P_{abs}/P_{las})]$ shown in Fig. 6(c). Combining the dependences of P_{rad}/P_{abs} and CE_P on I_{laser}, we see that increasing laser intensity can yield a significant increase in absolute in-band radiation without significantly influencing the conversion efficiency of the system.

V. SUMMARY AND CONCLUSION

In summary, we have investigated the power partitioning in a laser-produced tin plasma for laser wavelengths in the $1.064 \leq \lambda_{laser} \leq 10.6 \, \mu$m range and laser intensities of $0.5 \times 10^{11} \leq I_{laser} \leq 5 \times 10^{11}$ W cm^{-2} for $\lambda_{laser} = 1.064 \, \mu$m. We have identified a strong laser-wavelength dependence of laser absorptivity and the location of EUV generation. With increasing laser wavelength, the power balance monotonically shifts from kinetic losses to in-band radiative losses. The decrease in laser absorption for long laser wavelengths, combined with a concurrent decrease in EUV optical depth, yields a non-monotonic behavior of the conversion efficiency, leading to an optimum at $\lambda_{laser} = 4 \, \mu$m. EUV sources based on long laser wavelengths would, therefore, benefit from additional target preparation to ensure a higher absorption fraction. The influence of laser intensity on the power partitioning for $\lambda_{laser} = 1.064 \, \mu$m is found to be small: no significant shift between kinetic losses and radiative losses is seen. With increasing laser intensity, we find an increase in in-band radiative power at minor cost in terms of conversion efficiency.

ACKNOWLEDGMENTS

AUTHOR DECLARATIONS
Conflict of Interest

The authors have no conflicts to disclose.

Author Contributions

Diko J. Hemminga: Formal analysis (lead); Investigation (lead); Visualization (lead); Writing – original draft (lead). **Oscar Oreste Versolato:** Conceptualization (equal); Funding acquisition (lead); Project administration (equal); Supervision (supporting); Writing – review & editing (supporting). **John Sheil:** Conceptualization (equal); Project administration (equal); Supervision (lead);Writing – review & editing (lead).

DATA AVAILABILITY

The data that support the findings of this study are available from the corresponding author upon reasonable request.

REFERENCES

[1]S. K. Moore, IEEE Spectrum **55**, 46 (2018).

[2]*EUV Lithography*, 2nd ed., edited by V. Bakshi (SPIE Press, 2018).

[3]I. Fomenkov, D. Brandt, A. Ershov, A. Schafgans, Y. Tao, G. Vaschenko, S. Rokitski, M. Kats, M. Vargas, M. Purvis, R. Rafac, B. La Fontaine, S. De Dea, A. LaForge, J. Stewart, S. Chang, M. Graham, D. Riggs, T. Taylor, M. Abraham, and D. Brown, Adv. Opt. Technol. **6**, 173 (2017).

[4]S. Bajt, J. B. Alameda, T. W. Barbee, Jr., W. M. Clift, J. A. Folta, B. Kaufmann, and E. A. Spiller, Opt. Eng. **41**, 1797 (2002).

[5]Q. Huang, V. Medvedev, R. van de Kruijs, A. Yakshin, E. Louis, and F. Bijkerk, Appl. Phys. Rev. **4**, 011104 (2017).

[6]S. Fujioka, M. Shimomura, Y. Shimada, S. Maeda, H. Sakaguchi, Y. Nakai, T. Aota, H. Nishimura, N. Ozaki, A. Sunahara, K. Nishihara, N. Miyanaga, Y. Izawa, and K. Mima, Appl. Phys. Lett. **92**, 241502 (2008).

[7]K. Nishihara, A. Sunahara, A. Sasaki, M. Nunami, H. Tanuma, S. Fujioka, Y. Shimada, K. Fujima, H. Furukawa, T. Kato, F. Koike, R. More, M. Murakami, T. Nishikawa, V. Zhakhovskii, K. Gamata, A. Takata, H. Ueda, H. Nishimura, Y. Izawa, N. Miyanaga, and K. Mima, Phys. Plasmas **15**, 056708 (2008).

[8]J. Fujimoto, H. Mizoguchi, T. Abe, S. Tanaka, T. Ohta, T. Hori, T. Yanagida, and H. Nakarai, J. Micro/Nanolithogr., MEMS, MOEMS **11**, 021111 (2012).

[9]D. Kurilovich, A. L. Klein, F. Torretti, A. Lassise, R. Hoekstra, W. Ubachs, H. Gelderblom, and O. O. Versolato, Phys. Rev. Appl. **6**, 014018 (2016).

[10]S. Y. Grigoryev, B. Lakatosh, M. Krivokorytov, V. Zhakhovsky, S. Dyachkov, D. Ilnitsky, K. Migdal, N. Inogamov, A. Y. Vinokhodov, V. Kompanets, Y. V. Sidelnikov, V. Krivtsun, K. Koshelev, and V. Medvedev, Phys. Rev. Appl. **10**, 064009 (2018).

[11]J. Hernandez-Rueda, B. Liu, D. J. Hemminga, Y. Mostafa, R. A. Meijer, D. Kurilovich, M. Basko, H. Gelderblom, J. Sheil, and O. O. Versolato, Phys. Rev. Res. **4**, 013142 (2022).

[12]O. O. Versolato, Plasma Sources Sci. Technol. **28**, 083001 (2019).

[13]W. Svendsen and G. O'Sullivan, Phys. Rev. A **50**, 3710 (1994).

[14]S. S. Churilov and A. N. Ryabtsev, Phys. Scr. **73**, 614 (2006).

[15]S. Fujioka, H. Nishimura, K. Nishihara, A. Sasaki, A. Sunahara, T. Okuno, N. Ueda, T. Ando, Y. Tao, Y. Shimada, K. Hashimoto, M. Yamaura, K. Shigemori, M. Nakai, K. Nagai, T. Norimatsu, T. Nishikawa, N. Miyanaga, Y. Izawa, and K. Mima, Phys. Rev. Lett. **95**, 235004 (2005).

[16]A. Sasaki, A. Sunahara, H. Furukawa, K. Nishihara, S. Fujioka, T. Nishikawa, F. Koike, H. Ohashi, and H. Tanuma, J. Appl. Phys. **107**, 113303 (2010).

[17]G. O'Sullivan, B. Li, R. D'Arcy, P. Dunne, P. Hayden, D. Kilbane, T. McCormack, H. Ohashi, F. O'Reilly, P. Sheridan, E. Sokell, C. Suzuki, and T. Higashiguchi, J. Phys. B **48**, 144025 (2015).

[18]J. Scheers, C. Shah, A. Ryabtsev, H. Bekker, F. Torretti, J. Sheil, D. A. Czapski, J. C. Berengut, W. Ubachs, J. R. C. López-Urrutia, R. Hoekstra, and O. O. Versolato, Phys. Rev. A **101**, 062511 (2020).

[19]F. Torretti, J. Sheil, R. Schupp, M. M. Basko, M. Bayraktar, R. A. Meijer, S. Witte, W. Ubachs, R. Hoekstra, O. O. Versolato, A. J. Neukirch, and J. Colgan, Nat. Commun. **11**, 2334 (2020).

[20]I. V. Fomenkov, M. A. Purvis, A. A. Schafgans, Y. Tao, S. Rokitski, J. Stewart, A. LaForge, A. I. Ershov, R. J. Rafac, S. D. Dea, C. Rajyaguru, G. O. Vaschenko, M. Abraham, D. C. Brandt, and D. J. Brown, in *International Conference on Extreme Ultraviolet Lithography*, edited by K. G. Ronse, E. Hendrickx, P. P. Naulleau, P. A. Gargini, and T. Itani (SPIE, 2018).

[21]D. C. Brandt, M. Purvis, I. Fomenkov, D. Brown, A. Schafgans, P. Mayer, and R. Rafac, in *Extreme Ultraviolet (EUV) Lithography XII*, edited by N. M. Felix, A. Lio, D. C. Brandt, M. Purvis, I. Fomenkov, D. Brown, A. Schafgans, P. Mayer, and R. Rafac, [International Society for Optics and Photonics (SPIE), 2021].

[22]K. Nowak, T. Ohta, T. Suganuma, J. Fujimoto, H. Mizoguchi, A. Sumitani, and A. Endo, Opto-Electron. Rev. **21**, 345 (2013).

[23]I. Tamer, B. A. Reagan, T. Galvin, J. Galbraith, E. Sistrunk, A. Church, G. Huete, H. Neurath, and T. Spinka, Opt. Lett. **46**, 5096 (2021).

[24]T. Sizyuk and A. Hassanein, Phys. Plasmas **27**, 103507 (2020).

[25]R. Schupp, L. Behnke, J. Sheil, Z. Bouza, M. Bayraktar, W. Ubachs, R. Hoekstra, and O. O. Versolato, Phys. Rev. Res. **3**, 013294 (2021).

[26]Y. Yuan, Y. Y. Ma, W. P. Wang, S. J. Chen, Y. Cui, M. Zi, X. H. Yang, G. B. Zhang, and Y. X. Leng, Plasma Phys. Controlled Fusion **64**, 025001 (2021).

[27]C. W. Siders, A. C. Erlandson, T. C. Galvin, H. Frank, S. Langer, B. A. Reagan, H. Scott, E. F. Sistrunk, and T. M. Spinka, in *Source Workshop* (EUV Litho Inc., 2019).

[28]S. Fujioka, H. Nishimura, K. Nishihara, M. Murakami, Y.-G. Kang, Q. Gu, K. Nagai, T. Norimatsu, N. Miyanaga, Y. Izawa, and K. Mima, Appl. Phys. Lett. **87**, 241503 (2005).

[29]D. J. Hemminga, L. Poirier, M. M. Basko, R. Hoekstra, W. Ubachs, O. O. Versolato, and J. Sheil, Plasma Sources Sci. Technol. **30**, 105006 (2021).

[30]R. Schupp, F. Torretti, R. A. Meijer, M. Bayraktar, J. Sheil, J. Scheers, D. Kurilovich, A. Bayerle, A. A. Schafgans, M. Purvis, K. S. E. Eikema, S. Witte, W. Ubachs, R. Hoekstra, and O. O. Versolato, Appl. Phys. Lett. **115**, 124101 (2019).

[31]F. Torretti, F. Liu, M. Bayraktar, J. Scheers, Z. Bouza, W. Ubachs, R. Hoekstra, and O. Versolato, J. Phys. D **53**, 055204 (2019).

[32]M. M. Basko, V. G. Novikov, and A. S. Grushin, Phys. Plasmas **22**, 053111 (2015).

[33]M. Basko, Phys. Plasmas **23**, 083114 (2016).

[34]S. Langer, C. Siders, T. Galvin, H. Scott, and E. Sistrunk, in *Source Workshop* (EUV Litho Inc., 2019).

[35]I. Fomenkov, in *Source Workshop* (EUV Litho Inc., 2019).

[36]M. Basko, J. Maruhn, and A. Tauschwitz, GSI Rep. **1**, 410 (2010).

[37]M. M. Basko, P. V. Sasorov, M. Murakami, V. G. Novikov, and A. S. Grushin, Plasma Phys. Controlled Fusion **54**, 055003 (2012).

[38]A. Tauschwitz, M. Basko, A. Frank, V. Novikov, A. Grushin, A. Blazevic, M. Roth, and J. Maruhn, High Energy Density Phys. **9**, 158 (2013).

[39]M. M. Basko, M. S. Krivokorytov, A. Y. Vinokhodov, Y. V. Sidelnikov, V. M. Krivtsun, V. V. Medvedev, D. A. Kim, V. O. Kompanets, A. A. Lash, and K. N. Koshelev, Laser Phys. Lett. **14**, 036001 (2017).

[40]D. Kurilovich, M. M. Basko, D. A. Kim, F. Torretti, R. Schupp, J. C. Visschers, J. Scheers, R. Hoekstra, W. Ubachs, and O. O. Versolato, Phys. Plasmas **25**, 012709 (2018).

[41]F. L. Addessio, J. R. Baumgardner, J. K. Dukowicz, N. L. Johnson, B. A. Kashiwa, R. M. Rauenzahn, and C. Zemach, "CAVEAT: A computer code for fluid dynamics problems with large distortion and internal slip," Report No. LA-10613-MS-Rev. 1, UC-32 (Los Alamos National Laboratory, 1992).

[42]E. Livne and A. Glasner, J. Comput. Phys. **58**, 59 (1985).

[43]M. M. Basko, J. Maruhn, and A. Tauschwitz, J. Comput. Phys. **228**, 2175 (2009).

[44] A. F. Nikiforov, V. G. Novikov, and V. B. Uvarov, *Quantum-Statistical Models of Hot Dense Matter: Methods for Computation Opacity and Equation of State*, Progress in Mathematical Physics (Birkhauser, 2005).

[45] I. Vichev, A. Solomyannaya, A. Grushin, and D. Kim, High Energy Density Phys. **33**, 100713 (2019).

[46] S. Faik, A. Tauschwitz, and I. Iosilevskiy, Comput. Phys. Commun. **227**, 117 (2018).

[47] R. M. More, K. H. Warren, D. A. Young, and G. B. Zimmerman, Phys. Fluids **31**, 3059 (1988).

[48] A. Kemp and J. M. ter Vehn, Nucl. Instrum. Methods **415**, 674 (1998).

[49] M. M. Basko and I. P. Tsygvintsev, Comput. Phys. Commun. **214**, 59 (2017).

[50] S. Elezier, *The Interaction of High-Power Lasers With Plasmas* (CRC Press, 2002).

[51] R. Schupp, F. Torretti, R. A. Meijer, M. Bayraktar, J. Scheers, D. Kurilovich, A. Bayerle, K. S. E. Eikema, S. Witte, W. Ubachs, R. Hoekstra, and O. O. Versolato, Phys. Rev. Appl. **12**, 014010 (2019).

[52] R. Schupp, L. Behnke, Z. Bouza, Z. Mazzotta, Y. Mostafa, A. Lassise, L. Poirier, J. Sheil, M. Bayraktar, W. Ubachs, R. Hoekstra, and O. O. Versolato, J. Phys. D **54**, 365103 (2021).

[53] Y. Shimada, H. Nishimura, M. Nakai, K. Hashimoto, M. Yamaura, Y. Tao, K. Shigemori, T. Okuno, K. Nishihara, T. Kawamura *et al.*, Appl. Phys. Lett. **86**, 051501 (2005).

[54] A. Z. Giovannini and R. S. Abhari, J. Appl. Phys. **114**, 033303 (2013).

[55] A. Z. Giovannini and R. S. Abhari, Appl. Phys. Lett. **104**, 194104 (2014).

[56] A. Z. Giovannini, N. Gambino, B. Rollinger, and R. S. Abhari, J. Appl. Phys. **117**, 033302 (2015).

[57] V. Sizyuk, A. Hassanein, and T. Sizyuk, J. Appl. Phys. **100**, 103106 (2006).

[58] L. Behnke, R. Schupp, Z. Bouza, M. Bayraktar, Z. Mazzotta, R. Meijer, J. Sheil, S. Witte, W. Ubachs, R. Hoekstra, and O. O. Versolato, Opt. Express **29**, 4475 (2021).

[59] K. Nishihara, A. Sasaki, A. Sunahara, and T. Nishikawa, *EUV Sources for Lithography*, edited by V. Bakshi (SPIE Press, Bellingham, WA, 2006), Vol. 149, Chap. 11, pp. 339–370.

[60] A. Sunahara and K. Tanaka, Fusion Eng. Des. **85**, 935 (2010).

[61] K. Nishihara, Jpn. J. Appl. Phys., Part 1 **21**, L571 (1982).

[62] N. Tanaka, M. Masuda, R. Deguchi, M. Murakami, A. Sunahara, S. Fujioka, A. Yogo, and H. Nishimura, Appl. Phys. Lett. **107**, 114101 (2015).

[63] T. Pütterich, R. Neu, R. Dux, A. D. Whiteford, M. G. O'Mullane, and ASDEX Upgrade Team, Plasma Phys. Controlled Fusion **50**, 085016 (2008).